

SOAR: Self-Correction for Optimal Alignment and Refinement in Diffusion Models

You Qin* Linqing Wang*† Hao Fei Roger Zimmermann Liefeng Bo
Qinglin Lu Chunyu Wang‡

* Equal contribution. † Project lead. ‡ Corresponding authors.

Abstract

The post-training pipeline for diffusion models currently has two stages: supervised fine-tuning (SFT) on curated data and reinforcement learning (RL) with reward models. A fundamental gap separates them. SFT optimizes the denoiser only on ground-truth states sampled from the forward noising process; once inference deviates from these ideal states, subsequent denoising relies on out-of-distribution generalization rather than learned correction, exhibiting the same *exposure bias* that afflicts autoregressive models, but accumulated along the denoising trajectory instead of the token sequence. RL can in principle address this mismatch, yet its terminal reward signal is sparse, suffers from credit-assignment difficulty, and risks reward hacking. We propose **SOAR** (Self-Correction for Optimal Alignment and Refinement), a bias-correction post-training method that fills this gap. Starting from a real sample, SOAR performs a single stop-gradient rollout with the current model, re-noises the resulting off-trajectory state, and supervises the model to steer back toward the original clean target. The method is on-policy, reward-free, and provides dense per-timestep supervision with no credit-assignment problem. On SD3.5-Medium, SOAR improves GenEval from 0.70 to 0.78 and OCR from 0.64 to 0.67 over SFT, while simultaneously raising all model-based preference scores. In controlled reward-specific experiments, SOAR surpasses Flow-GRPO in final metric value on both aesthetic and text-image alignment tasks, despite having no access to a reward model. Since SOAR’s base loss subsumes the standard SFT objective, it can directly replace SFT as a stronger first post-training stage after pretraining, while remaining fully compatible with subsequent RL alignment.

1 Introduction

Diffusion and flow-matching models have become the dominant paradigm for high-quality visual generation, powering text-to-image (Rombach et al., 2022; Esser et al., 2024; Labs, 2024), text-to-video (Kong et al., 2024), and 3D synthesis systems. Despite rapid progress in scaling and architecture, the *post-training* recipe for these generators remains far less mature than its counterpart in large language models. In current practice a model is first pretrained at scale, then fine-tuned on curated data (SFT), and optionally aligned with reward-based optimization (RL). Yet even strong models continue to suffer from recurring failures: wrong object counts, malformed hands, broken text rendering, and unstable identity preservation.

We argue that these failures share a common root: *exposure bias* in the denoising trajectory. In autoregressive language models, exposure bias refers to the mismatch between ground-truth-conditioned training and autoregressive inference (Bengio et al., 2015). Diffusion models suffer from the same phenomenon along a different axis. Standard SFT constructs noisy training states via the forward process of real data and optimizes the denoiser on these ideal, ground-truth states. During inference, however, the model conditions on its own earlier predictions. Once an early denoising step makes a small error, subsequent states enter regions that were not directly optimized; recovery then depends on out-of-distribution generalization rather than a learned correction mechanism. The error compounds over dozens of sampling steps and can become irreversible well before the final image is rendered.

A natural response is to apply preference-based or reward-based optimization. Offline methods such as Diffusion-DPO (Wallace et al., 2024) adapt direct preference optimization to diffusion models by learning from human-annotated image pairs, while online methods such as Flow-GRPO (Liu et al., 2025) convert the deterministic ODE sampler into a stochastic SDE and apply

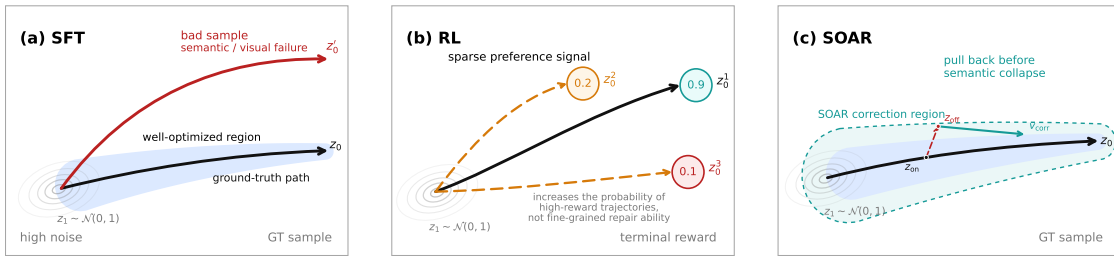


Figure 1: Conceptual comparison of post-training regimes from a trajectory perspective. **Left: SFT** trains only on ground-truth denoising states. Once an inference rollout exits the narrow corridor of well-optimized states, subsequent steps sharpen the wrong structure. **Middle: RL** separates good and bad final outcomes with a terminal reward, but the sparse signal arrives after the erroneous rollout has already formed. **Right: SOAR** performs a one-step rollout to generate off-trajectory states and supervises the model to correct back toward the clean target, acting before semantic errors fully materialize.

policy-gradient exploration, achieving impressive improvements on compositional benchmarks. Similarly, DiffusionNFT (Zheng et al., 2026) contrasts reward-split positive and negative generations on the forward process to define an implicit policy improvement direction. However, these approaches share fundamental challenges: the preference or reward signal is sparse and terminal, only available after a complete rollout, making credit assignment across dozens of denoising steps difficult. Aggressive single-reward optimization also risks reward hacking, where the model improves the targeted metric at the cost of diversity or other quality dimensions (Liu et al., 2025).

This paper proposes **SOAR** (Self-Correction for Optimal Alignment and Refinement), a post-training method that replaces SFT as a stronger first stage directly following pretraining, while remaining fully compatible with subsequent RL alignment. The core idea is simple: instead of waiting for a terminal reward after a full rollout, we directly teach the model how to correct its own trajectory errors at the timestep where they occur. Starting from a real training pair, SOAR performs a single stop-gradient ODE step with the current model to generate an off-trajectory state, re-noises this state to multiple auxiliary noise levels, and supervises the denoiser to steer each auxiliary state back toward the original clean target. The resulting training signal is *on-policy*, since the off-trajectory states evolve with the model’s own parameters; *dense*, as the correction target is derived from the ground-truth sample itself rather than collapsed into a scalar reward or a relative preference; and *reward-free*, requiring no external reward model or preference annotation. The correction target is derived analytically from the training pair, eliminating the credit-assignment problem entirely.

Placing SOAR in the landscape of existing post-training paradigms clarifies its role. SFT trains exclusively on ground-truth denoising states; it is off-policy by construction because the model never sees its own inference-time errors during training. RL-based methods introduce on-policy or reward-driven signals but share common limitations: the supervision is sparse and terminal, credit must be assigned across dozens of denoising steps, and aggressive single-reward optimization risks reward hacking. By design, SOAR is free from all of these limitations. Moreover, when the training corpus is curated according to a target preference, such as filtering for high aesthetic or high text-image alignment, SOAR can absorb that preference while preserving quality on other dimensions, since its dense ground-truth supervision leaves no room for reward hacking. In the current work we position SOAR as a first-stage replacement for SFT that seamlessly connects with subsequent RL alignment; however, our experiments on preference-curated subsets already demonstrate its potential as a data-efficient alternative to RL-based optimization itself. We summarize the key differences among these paradigms in Table 1.

Table 1: Qualitative comparison of post-training paradigms for diffusion models. SOAR combines on-policy training with dense, reward-free supervision while maintaining low training cost.

	Training Signal	On-policy	Signal Density	Reward Model	Credit Assign.	Reward Hacking	Resolves Model Bias	Training Cost
SFT	Supervised (GT traj.)	✗	Dense	✗	✗	✗	✗	Low
DPO	Pref. pairs (implicit reward)	✗	Sparse	✗	✗	✗	Partial	Medium
RL	Reward function	✓	Sparse	✓	✓	✓	Partial	High
SOAR	Supervised (traj. correction)	✓ (single-step)	Dense	✗	✗	✗	✓	Low

Our main contributions are:

- We identify exposure bias, the distributional mismatch between ground-truth training states and model-induced inference states, as a unifying explanation for many persistent diffusion generation failures.
- We propose SOAR, a practical post-training algorithm that constructs off-trajectory states via a single ODE rollout, re-noises them, and optimizes the model with an analytically derived correction target anchored to the original clean sample.
- We provide a controlled experimental comparison showing that SOAR improves both rule-based (GenEval, OCR) and model-based (PickScore, ClipScore, HPSv2.1, Aesthetic, ImageReward) metrics simultaneously over SFT, achieving monotonic reward improvement without a reward model.
- We show that on curated high-reward data subsets, SOAR outperforms both vanilla SFT and explicit RL (Flow-GRPO) in final metric value, validating the trajectory-correction paradigm as a data-efficient alternative to reward optimization.

2 Methodology

2.1 Preliminaries: Flow Matching

Let $z_0 \sim q(z_0)$ denote a clean latent sampled from the data distribution and $z_1 \sim \mathcal{N}(0, I)$ denote Gaussian noise. Rectified flow (Liu et al., 2023; Esser et al., 2024) defines a linear interpolation path between data and noise:

$$z_t = (1 - t)z_0 + tz_1, \quad t \in [0, 1], \quad (1)$$

where we use t (or equivalently the scheduler value σ_t) to index the noise level. A neural network $v_\theta(z_t, c, t)$ is trained to predict the velocity field by minimizing the flow matching objective:

$$\mathcal{L}_{\text{FM}}(\theta) = \mathbb{E}_{z_0, z_1, c, t} [\|v_\theta(z_t, c, t) - (z_1 - z_0)\|^2]. \quad (2)$$

Given a trained velocity field, sampling proceeds by solving the ODE from $t=1$ (pure noise) to $t=0$ (clean data). With Euler discretization over K steps, each update reads

$$z_{t-\Delta t} = z_t + \Delta t \cdot v_\theta(z_t, c, t), \quad \Delta t = -1/K. \quad (3)$$

The velocity prediction at any state z and noise level σ implies a *clean-endpoint estimate*:

$$\hat{z}_0(z, \sigma) = z - \sigma \cdot v_\theta(z, c, \sigma). \quad (4)$$

This map will play a central role in the correction objective below.

2.2 Post-Training Paradigms

Supervised fine-tuning (SFT). Given a curated dataset of (z_0, c) pairs, SFT continues to minimize the flow matching loss in Eq. equation 2. The training states z_t are constructed by the forward process of real samples: $z_t = (1-t)z_0 + tz_1$ with fresh noise $z_1 \sim \mathcal{N}(0, I)$. This means SFT only optimizes the model on the *ground-truth* state distribution

$$p_t^{\text{data}}(z) = \int \delta((1-t)z_0 + tz_1)(z) q(z_0) \mathcal{N}(z_1) dz_0 dz_1. \quad (5)$$

During inference, however, the model generates states from a different distribution $p_t^\theta(z)$, defined implicitly by the ODE rollout from z_1 through the learned velocity field. Since each state depends

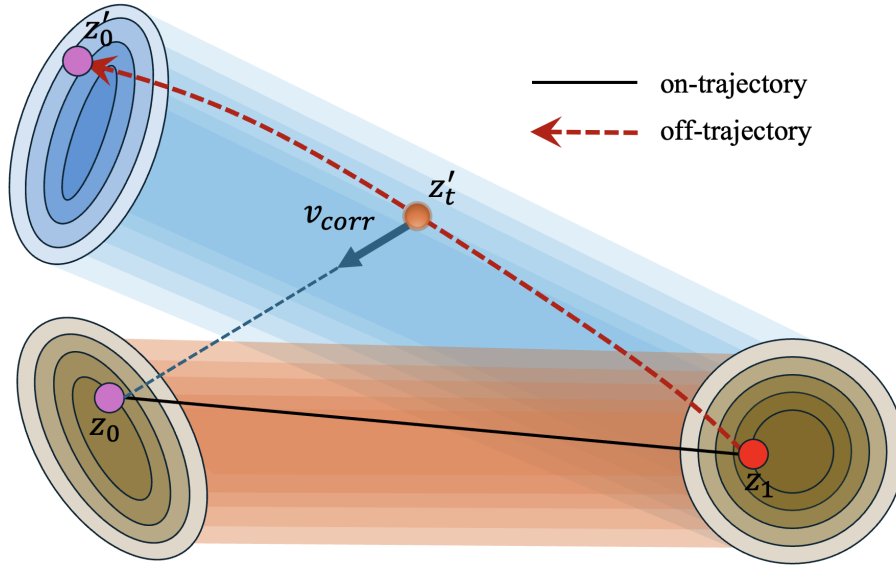


Figure 2: Noise-level analysis illustrating the ideal trajectory, the biased rollout, and the local correction direction. The off-trajectory state is constructed by one ODE step with the current model and then re-noised to auxiliary levels.

on the model’s previous predictions, early errors propagate and push later states into regions where the model was never directly trained. This train–inference mismatch is the *exposure bias* of diffusion models: the same phenomenon that affects autoregressive generation (Bengio et al., 2015), but accumulated along the denoising trajectory instead of the token sequence.

Reward-based alignment and RL. To improve beyond SFT, recent work explores reward-driven optimization for diffusion and flow-matching models. Approaches range from offline preference learning such as DPO (Wallace et al., 2024), which adjusts the relative likelihood of preferred and dispreferred samples, to online policy-gradient methods. Among the latter, Flow-GRPO (Liu et al., 2025) is representative: it converts the deterministic ODE sampler into an equivalent SDE that preserves the marginal distribution at all timesteps, enabling stochastic exploration, and applies group-relative policy optimization (GRPO) where a group of G images is generated per prompt, scored by a reward function $r(z_0, c)$, and the normalized group advantage $\hat{A}^i = (r^i - \bar{r}) / \text{std}(r)$ drives a clipped policy-gradient update. While Flow-GRPO achieves strong results on compositional benchmarks (GenEval 0.63→0.95), RL-based approaches share inherent limitations: (i) the reward signal is sparse and terminal, arriving only after the full denoising trajectory is complete; (ii) credit assignment across dozens of denoising steps is difficult; (iii) aggressive single-reward optimization risks reward hacking, where the targeted metric improves at the cost of diversity or other quality dimensions.

2.3 SOAR: Trajectory Bias Correction

SOAR addresses the exposure bias directly: instead of patching failures after a full rollout, it teaches the model to correct trajectory errors at the timestep where they occur.

2.3.1 Distributional Mismatch

SFT minimizes the velocity error over ground-truth states $z \sim p_t^{\text{data}}$ (Eq. 5). At inference time the model instead encounters states $z \sim p_t^\theta$, the distribution induced by its own ODE rollout. Because each sampled state is produced from the model’s previous prediction, even small local velocity errors can move the trajectory away from the ground-truth path, and the resulting deviation compounds across subsequent denoising steps. SOAR closes this gap by explicitly constructing states that approximate p_t^θ during training and supervising the model on them.

2.3.2 Constructing Off-Trajectory States

Given a training pair (z_0, c) and sampled noise $z_1 \sim \mathcal{N}(0, I)$, we construct the on-trajectory state at a sampled time t_0 :

$$z_{\sigma_{t_0}} = (1 - \sigma_{t_0}) z_0 + \sigma_{t_0} z_1. \quad (6)$$

We then simulate what the model would produce during inference by running a single *stop-gradient* ODE step with classifier-free guidance (CFG). Concretely, we compute a detached CFG velocity $v_{\text{cfg}} = \text{sg}[v_{\text{uncond}} + w_{\text{cfg}}(v_{\text{cond}} - v_{\text{uncond}})]$ at the shared state $z_{\sigma_{t_0}}$, and define the next timestep $t_1 = \max(t_0 - 1/K, 0)$. One Euler step produces the off-trajectory state:

$$\hat{z}_{\sigma_{t_1}} = z_{\sigma_{t_0}} + (\sigma_{t_1} - \sigma_{t_0}) v_{\text{cfg}}. \quad (7)$$

This is the model’s own prediction; it deviates from the ideal state $(1 - \sigma_{t_1})z_0 + \sigma_{t_1}z_1$ in exactly the way that inference would.

To generate diverse auxiliary supervision, we *re-noise* this off-trajectory state by interpolating it back toward the noise endpoint z_1 . For N uniformly sampled auxiliary noise levels $\sigma_{t'} \sim \text{Uniform}[\sigma_{t_1}, 1]$, we set $\alpha = (\sigma_{t'} - \sigma_{t_1}) / (1 - \sigma_{t_1})$ and construct:

$$z_{\sigma_{t'}} = (1 - \alpha) \hat{z}_{\sigma_{t_1}} + \alpha z_1. \quad (8)$$

A key design choice is that re-noising uses the **same** z_1 as the base loss. This keeps the auxiliary state in the neighborhood of the original transport ray $z_0 \leftrightarrow z_1$: the deviation from the ideal path is $(1 - \alpha)$ times the one-step rollout error, which is bounded and shrinks as $\alpha \rightarrow 1$. Consequently, z_0 remains the uniquely correct clean-endpoint target for these nearby off-trajectory states, and the correction direction has a clear geometric meaning along the conditional interpolation path (see Appendix A for the formal argument).

2.3.3 Correction Objective

The most natural way to correct a drifted trajectory is *local trajectory matching*: require that, after a small step Δt , the off-trajectory state reconverges with the on-trajectory state:

$$z_{\sigma} + \Delta t \cdot v_{\text{gt}} = z'_{\sigma} + \Delta t \cdot v_{\text{corr}}, \quad (9)$$

where z_{σ} is the on-trajectory state and z'_{σ} is the off-trajectory state at the same noise level. This ensures the corrected path returns to the ideal trajectory after one step. However, the step size Δt introduces an ambiguity: different Δt yield different targets, and the optimal choice depends on the downstream trajectory, making it impractical in a multi-step ODE.

We resolve this by requiring both states to reach the same *final* endpoint z_0 . On the ideal trajectory, the on-trajectory state $z_{\sigma} = (1 - \sigma)z_0 + \sigma z_1$ with velocity $v_{\text{gt}} = z_1 - z_0$ satisfies

$$z_{\sigma} - \sigma \cdot v_{\text{gt}} = z_0. \quad (10)$$

We impose the same *goal consistency* condition on the off-trajectory state. Since z'_{σ} remains close to the original trajectory by construction (Section 2.3.2), the clean target z_0 is still the correct destination:

$$z'_{\sigma} - \sigma \cdot v_{\text{corr}} = z_0. \quad (11)$$

Solving for v_{corr} yields the closed-form correction target:

$$v_{\text{corr}} = \frac{z'_{\sigma} - z_0}{\sigma}. \quad (12)$$

This eliminates the Δt ambiguity: the target depends only on the current state and the clean anchor z_0 . When $z'_{\sigma} = z_{\sigma}$ (no deviation), it reduces exactly to $v_{\text{gt}} = z_1 - z_0$, recovering the standard flow matching target. When $z'_{\sigma} \neq z_{\sigma}$, $v_{\text{corr}} - v_{\text{gt}} = (z'_{\sigma} - z_{\sigma}) / \sigma$ is a correction proportional to the rollout deviation, steering the model back toward z_0 from the off-trajectory states it actually visits during inference. This is the dense, per-timestep signal that SFT cannot provide.

The total SOAR objective combines the on-trajectory base loss with the auxiliary correction loss. Concretely, for a batch of B samples with N auxiliary points each:

$$\mathcal{L}_{\text{base}} = \sum_{b=1}^B w(\sigma_{t_0}^{(b)}) \|v_{\theta}(z_{\sigma_{t_0}}^{(b)}, c, t_0) - v_{\text{gt}}^{(b)}\|^2, \quad (13)$$

$$\mathcal{L}_{\text{corr}} = \sum_{p=1}^P w(\sigma_{t'}^{(p)}) \|v_{\theta}(z_{\sigma_{t'}}^{(p)}, c, t') - v_{\text{corr}}^{(p)}\|^2, \quad (14)$$

Algorithm 1 SOAR training (ODE-only, default configuration)

Require: velocity field v_θ , CFG scale w_{cfg} , step count K , aux count N , weight λ

- 1: **for** each training batch (z_0, c) **do**
- 2: Sample $z_1 \sim \mathcal{N}(0, I)$, sample time t_0 , compute σ_{t_0}
- 3: $z_{\sigma_{t_0}} \leftarrow (1 - \sigma_{t_0})z_0 + \sigma_{t_0}z_1$ ▷ on-trajectory state
- 4: $v_{\text{on}} \leftarrow v_\theta(z_{\sigma_{t_0}}, c, t_0)$; $v_{\text{gt}} \leftarrow z_1 - z_0$
- 5: Accumulate $\mathcal{L}_{\text{base}} \leftarrow w(\sigma_{t_0})\|v_{\text{on}} - v_{\text{gt}}\|^2$
- 6: $v_{\text{cfg}} \leftarrow \text{sg}[v_{\text{uncond}} + w_{\text{cfg}}(v_{\text{cond}} - v_{\text{uncond}})]$
- 7: $t_1 \leftarrow \max(t_0 - 1/K, 0)$; $\sigma_{t_1} \leftarrow \sigma(t_1)$
- 8: $\hat{z}_{\sigma_{t_1}} \leftarrow z_{\sigma_{t_0}} + (\sigma_{t_1} - \sigma_{t_0})v_{\text{cfg}}$ ▷ one ODE step
- 9: **for** $n = 1, \dots, N$ **do**
- 10: Sample $\sigma_{t'} \sim \text{Uniform}[\sigma_{t_1}, 1]$
- 11: $\alpha \leftarrow (\sigma_{t'} - \sigma_{t_1}) / (1 - \sigma_{t_1})$
- 12: $z_{\sigma_{t'}} \leftarrow (1 - \alpha)\hat{z}_{\sigma_{t_1}} + \alpha z_1$ ▷ re-noise with same z_1
- 13: $v_{\text{off}} \leftarrow v_\theta(z_{\sigma_{t'}}, c, t')$
- 14: $v_{\text{corr}} \leftarrow (z_{\sigma_{t'}} - z_0) / \sigma_{t'}$
- 15: Accumulate $\mathcal{L}_{\text{corr}} += w(\sigma_{t'})\|v_{\text{off}} - v_{\text{corr}}\|^2$
- 16: **end for**
- 17: $\mathcal{L}_{\text{SOAR}} \leftarrow (\mathcal{L}_{\text{base}} + \lambda \mathcal{L}_{\text{corr}}) / (1 + \lambda N)$ ▷ normalized
- 18: Update θ using $\nabla_\theta \mathcal{L}_{\text{SOAR}}$
- 19: **end for**

where P is the total number of valid auxiliary points. The combined objective is normalized by the total count of supervised items (synchronized across distributed workers):

$$\mathcal{L}_{\text{SOAR}} = \frac{\mathcal{L}_{\text{base}} + \lambda \mathcal{L}_{\text{corr}}}{B + \lambda P}. \quad (15)$$

From a distribution-matching perspective, both terms minimize the 2-Wasserstein distance between the model’s clean-endpoint prediction and the true z_0 , but the expectation is now taken over $p^{\text{data}} \cup p^{\text{rollout}}$ instead of p^{data} alone, directly closing the exposure-bias gap (Appendix A.4).

Unlike reward-based post-training, SOAR does not wait until a full sample is generated and then ask an external reward model to score the outcome. It operates directly at the denoising level and corrects trajectory bias where the failure first begins to form. A detailed comparison with SFT, DPO, and Flow-GRPO is provided in the Introduction; the full derivation of the correction target and the distribution-matching interpretation are given in Appendix A.

3 Experiments

3.1 Experimental Setup

Backbone and evaluation. All experiments use the SD3.5-Medium (Esser et al., 2024) backbone. Generated images are evaluated at 512×512 resolution with $\text{cfg}=4.5$. Our model-based metrics are evaluated on out-of-domain (OOD) DrawBench (Saharia et al., 2022). For rule-based metrics, GenEval (Huang et al., 2023) (compositional accuracy) and OCR (text rendering fidelity) are evaluated on the corresponding GenEval and OCR test sets from Flow-GRPO (Liu et al., 2025), following the evaluation protocol used by DiffusionNFT (Zheng et al., 2026). These test sets are used for evaluation only, not for training.

Training data. SOAR is trained on paired image–text data and requires no preference labels, reward annotations, or negative samples. The full training corpus contains **286,119** image–caption pairs. Because the correction target is anchored to the clean latent of a real sample, data quality is critical: noisy captions or semantically mismatched pairs would inject incorrect anchors into the supervision signal.

Broad-data comparison. Our primary experiment trains all methods on the **full 286K corpus** and compares them head-to-head across all metrics. The comparison set includes the SD3.5-M

Table 2: Main quantitative comparison at 512×512 (cfg=4.5). Rule-based metrics are evaluated on the Flow-GRPO test sets; model-based metrics are evaluated on OOD DrawBench. [†]Official checkpoint. [‡]At 1024×1024 . **Bold**: best overall; underline: second best.

Model	#Iter	Rule-Based (Flow-GRPO test sets)		Model-Based (OOD DrawBench)				
		GenEval	OCR	PickScore	ClipScore	HPSv2.1	Aesthetic	ImgRwd
SD-XL [†]	–	0.55	0.14	22.42	0.287	0.280	5.60	0.76
SD3.5-L [†]	–	0.71	0.68	22.91	0.289	0.288	5.50	0.96
FLUX.1-Dev [†]	–	0.66	0.59	22.84	0.295	0.274	5.71	0.96
SD3.5-M	–	0.63	0.59	22.34	0.285	0.279	5.36	0.85
+ SFT	10k	0.70	0.64	22.71	0.295	0.284	5.35	1.04
+ SOAR (Ours)	10k	0.78	0.67	22.86	0.295	0.289	5.46	1.09

pretrained baseline (no post-training), + SFT (full-parameter fine-tuning, 10k steps), and + SOAR (full-parameter trajectory-corrected fine-tuning, 10k steps). For context, we also report reference baselines from SD-XL (Podell et al., 2024), SD3.5-L (Esser et al., 2024), and FLUX.1-Dev (Labs, 2024). All runs use a global batch size of 512 and a constant learning rate of 2×10^{-5} . This setting directly measures whether trajectory correction improves general generation quality beyond what standard SFT achieves.

Reward-specific comparison. To isolate the effect of the training *objective* rather than data scale, we construct two curated subsets from the full corpus: a **High-Aesthetic** subset (aesthetic score ≥ 6.8 , 3,725 pairs) and a **High-ClipScore** subset (CLIP score ≥ 0.40 , 6,857 pairs). On each subset we compare three paradigms under identical compute (5k gradient steps, 128 GPUs, global batch size 32, constant learning rate 2×10^{-5}): SFT and SOAR both perform full-parameter fine-tuning with only an implicit reward signal from the curated data, while Flow-GRPO (Liu et al., 2025) explicitly optimizes the target reward via LoRA-based policy gradients with direct access to the reward model. Because all methods see the same high-quality data, any performance difference must come from the optimization paradigm itself, revealing which approach is more data-efficient and which is more prone to representation drift or reward hacking.

3.2 Main Results

Table 2 summarizes the broad-data comparison results. SOAR improves over SFT on *every* reported metric: on the Flow-GRPO test sets, GenEval rises from 0.70 to 0.78 (+11% relative) and OCR from 0.64 to 0.67; on OOD DrawBench, all five model-based scores improve simultaneously. The rule-based gains are particularly relevant because GenEval and OCR directly measure compositional accuracy and text-rendering fidelity, precisely the failure modes tied to early semantic decisions in the denoising trajectory, suggesting that trajectory-level correction prevents errors at high-noise stages from propagating into visible failures. Notably, the OOD DrawBench model-based improvements (PickScore +0.15, HPSv2.1 +0.005, Aesthetic +0.11, ImageReward +0.05 over SFT) are achieved *without* any reward model during training. On-trajectory denoising preserves the coherent global structure established at high-noise stages, and preference models implicitly reward this structural consistency when scoring the final image. Compared with reference models, SOAR on SD3.5-M surpasses the larger SD3.5-L on Flow-GRPO test-set GenEval (0.78 vs. 0.71) and OOD DrawBench HPSv2.1 (0.289 vs. 0.288), and approaches FLUX.1-Dev on OOD DrawBench PickScore (22.86 vs. 22.84), demonstrating that trajectory correction can close much of the gap between a medium-sized model and significantly larger architectures.

3.3 Reward-Specific Training Dynamics

We now turn to the reward-specific setting described in Section 3.1: SFT, SOAR, and Flow-GRPO are trained on the High-Aesthetic and High-ClipScore subsets under identical compute, contrasting implicit data-driven optimization against explicit RL. These subsets are used for training; Figure 3 reports the corresponding target metrics on the OOD DrawBench evaluation prompts across training steps.

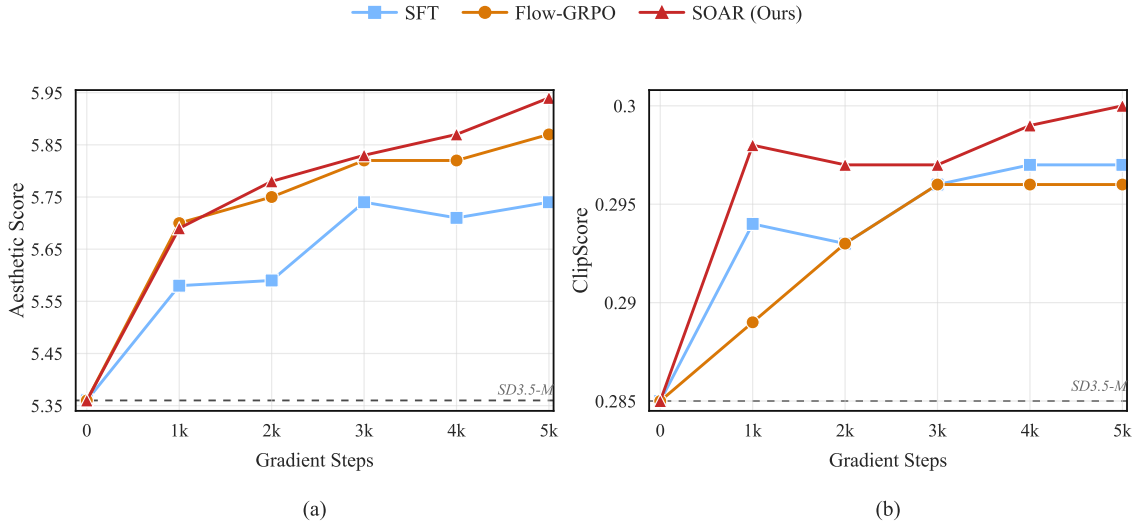


Figure 3: Reward-specific training dynamics at 512×512 . **(a)** OOD DrawBench Aesthetic score after training on the 3,725-pair High-Aesthetic subset (≥ 6.8). **(b)** OOD DrawBench ClipScore after training on the 6,857-pair High-ClipScore subset. All methods start from the same SD3.5-M pretrained checkpoint (step 0). SOAR achieves the highest final values in both settings with monotonic improvement.

SOAR achieves the highest reward with monotonic improvement. On OOD DrawBench, SOAR reaches the best final value at 5,000 steps in both reward-specific experiments, reaching 5.94 aesthetic score (vs. 5.74 for SFT, 5.87 for GRPO) and 0.300 ClipScore (vs. 0.297 for SFT, 0.296 for GRPO). Its improvement curve is *monotonic*: every checkpoint improves over the last, because the auxiliary correction loss regularizes the denoising trajectory and prevents representation drift. In contrast, SFT saturates early, jumping from the 5.36 baseline to 5.58 aesthetic at 1k steps but plateauing at 5.74 for the remaining 4k steps (ClipScore similarly plateaus at 0.297). This is consistent with the exposure-bias analysis: standard fine-tuning quickly absorbs the dominant data distribution at on-trajectory states but lacks a mechanism to further improve off-trajectory behavior, so additional training steps yield diminishing returns.

Explicit RL does not dominate implicit approaches. Perhaps surprisingly, Flow-GRPO, which has direct access to the reward model, does not reach the highest final value in either experiment. On aesthetics it achieves 5.87 (vs. SOAR’s 5.94); on ClipScore it reaches 0.296 (vs. SOAR’s 0.300). Two factors explain this: (i) GRPO updates only LoRA parameters (~ 75 MB vs. full model), limiting representational capacity; (ii) explicit reward optimization through RL is sample-inefficient compared with direct supervision on high-quality data; each RL gradient step requires generating multiple rollouts and computing rewards, whereas SOAR derives a dense correction signal analytically from each training pair.

GRPO trades off non-target metrics. Although GRPO improves the target aesthetic score, its ClipScore drops from 0.285 (baseline) to 0.277 at 5,000 steps, a 2.8% relative decline. In contrast, SFT and SOAR maintain or improve ClipScore while boosting aesthetics. This illustrates the well-known reward-hacking risk: aggressive single-reward optimization can degrade uncorrelated properties. SOAR avoids this pitfall entirely because it has no reward function to overfit to; its implicit “reward” is the data distribution itself, which naturally balances multiple quality dimensions.

These results motivate the staged pipeline proposed in this paper: first use SOAR to correct trajectory-level bias on broad data (improving general quality without reward hacking), then apply targeted reward optimization (e.g., GRPO) only when a specific metric deficit remains.

3.4 Ablation Study

We ablate key design choices of SOAR. All variants are trained for 10,000 steps on the full training set at 512×512 with $\text{cfg}=4.5$.

Table 3: Ablation of SOAR design choices on SD3.5-M (512×512 , $\text{cfg}=4.5$, 10k steps). Rule-based metrics use the Flow-GRPO test sets; model-based metrics use OOD DrawBench. Best per column in **bold**.

Variant	Rule-Based (Flow-GRPO test sets)		Model-Based (OOD DrawBench)				
	GenEval	OCR	PickScore	ClipScore	HPSv2.1	Aesthetic	ImgRwd
SOAR (ODE-only, shared z_1)	0.78	0.67	22.86	0.295	0.289	5.46	1.09
+ SDE branch	0.78	0.65	22.87	0.296	0.287	5.47	1.07
+ random z_1 per path	0.76	0.64	22.89	0.292	0.287	5.45	1.08

ODE-only vs. ODE+SDE branches. Beyond the deterministic ODE step described in Section 2.3.2, one can construct additional stochastic rollout branches via SDE samplers (e.g., coefficient-preserving sampling). We compare the default ODE-only configuration ($M=1$) against 1 ODE + 1 SDE branch ($M=2$). As shown in Table 3, removing the SDE branch slightly improves GenEval (tied at 0.78), OCR (0.67 vs. 0.65), HPSv2.1 (0.289 vs. 0.287), and ImageReward (1.09 vs. 1.07), while other metrics remain comparable. For the current training budget, the deterministic ODE path alone supplies sufficiently diverse off-trajectory states for bias correction. The ODE-only variant also halves the auxiliary compute cost per training step, making it the more practical default.

Shared z_1 vs. fresh random z_1 . The default SOAR re-noises off-trajectory states using the **same** z_1 drawn for the base loss, keeping auxiliary states on the same interpolation path (Section 2.3.2). An alternative draws independent Gaussian noise for each auxiliary path. Fresh z_1 slightly degrades rule-based metrics (GenEval 0.76, OCR 0.64) but yields the highest PickScore (22.89). The degradation in compositional accuracy confirms the geometric argument from Section 2.3.2: reusing the original z_1 keeps the auxiliary states close to the actual forward-process distribution and maintains the validity of z_0 as the correction anchor. Random noise introduces more diverse but noisier supervision where the anchor assumption weakens, which may require longer training or careful weighting to match the default.

A full sweep of the rollout-path count M , auxiliary-point count N , step count K , and noise weighting $w(\sigma)$ is deferred to an extended version.

3.5 In-Depth Analysis

We discuss several important questions about the design assumptions and practical implications of SOAR.

Q1: Is z_0 always the correct correction target for off-trajectory states? The correction loss directs the model toward the original training sample z_0 regardless of how far the rollout has drifted. In principle, an off-trajectory state z_{σ_t} could be legitimately denoised to a different clean sample z'_0 that is more consistent with its current latent structure. SOAR’s assumption is that the deviation is small enough, bounded by a single ODE step, so that z_0 remains the most plausible target. This assumption is strongest at low noise levels, where the latent is already close to z_0 and the set of plausible clean endpoints is narrow. At high noise levels, the assumption is less obvious but still supported by two factors: (i) the one-step rollout deviation is proportional to $1/K$, which is small relative to the total trajectory; (ii) re-noising with the shared z_1 preserves proximity to the original transport ray (Appendix A.3). The deliberate choice of $K=1$ rollout step keeps the deviation bounded and is a key design safeguard.

Q2: Why does high-noise correction improve semantics but not aesthetics? GenEval and OCR (semantic accuracy) improve substantially, while Aesthetic Score and PickScore (perceptual quality) improve only modestly. This follows from a noise-regime analysis: semantic decisions such as object count, spatial arrangement, and text layout are made at high-noise stages where the latent is ambiguous, whereas low-noise stages refine texture and detail. SOAR’s correction has the largest impact at high noise, where the off-trajectory deviation is largest. In effect, high-noise correction trains the model to reach the correct semantic structure from a wider range of initial noise samples z_1 , functioning similarly to “golden initial noise” selection but at training time rather than inference time.

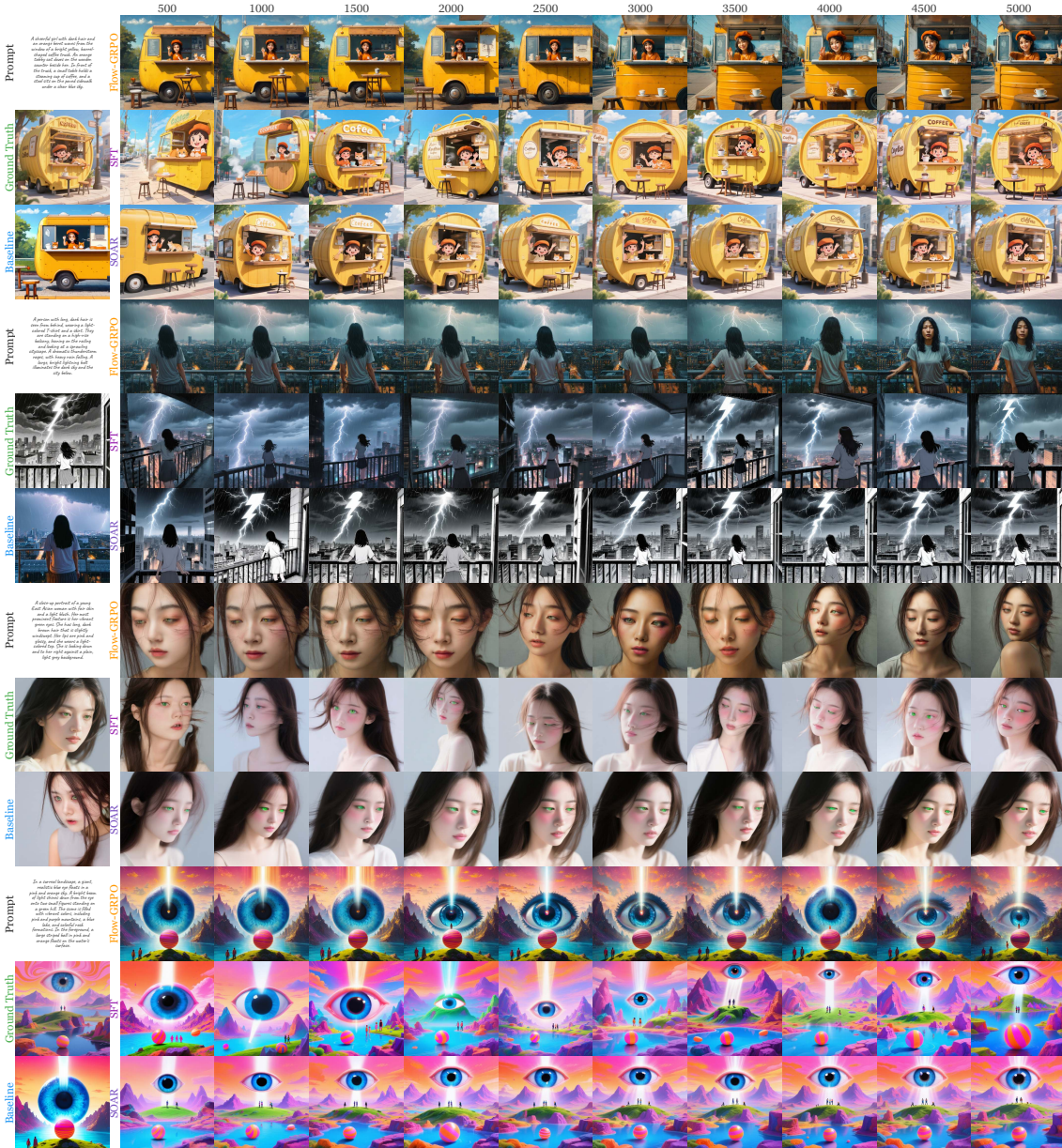


Figure 4: Training visualization on the **high-aesthetic** subset, covering portraits, landscapes, and anime styles. SOAR rapidly acquires coherent composition and structural fidelity as training progresses.

Q3: Does trajectory correction reduce generation diversity? Trajectory correction may reduce diversity at high-noise levels by narrowing the set of initial noise realizations that lead to semantically valid outputs. However, we argue that this is a desirable trade-off rather than a deficiency. Unconstrained diversity in diffusion models includes outputs with wrong object counts, malformed anatomy, and broken text, i.e., semantically invalid samples that no user wants. What matters in practice is *diversity under semantic consistency*: the range of valid, high-quality outputs the model can produce for a given prompt. By teaching the denoiser to stay on-trajectory, SOAR eliminates the portion of the output space that corresponds to off-trajectory failures while preserving the legitimate variation encoded in the training distribution. In this sense, trajectory correction acts as a semantic consistency constraint that channels the model’s capacity toward meaningful diversity rather than erratic noise-dependent failures. A thorough quantitative evaluation of this trade-off, with per-prompt LPIPS variance and distribution-level Vendi Score, is planned for future work.



Figure 5: Training visualization on poster data. SOAR learns layout structure, typographic placement, and visual hierarchy with high fidelity.

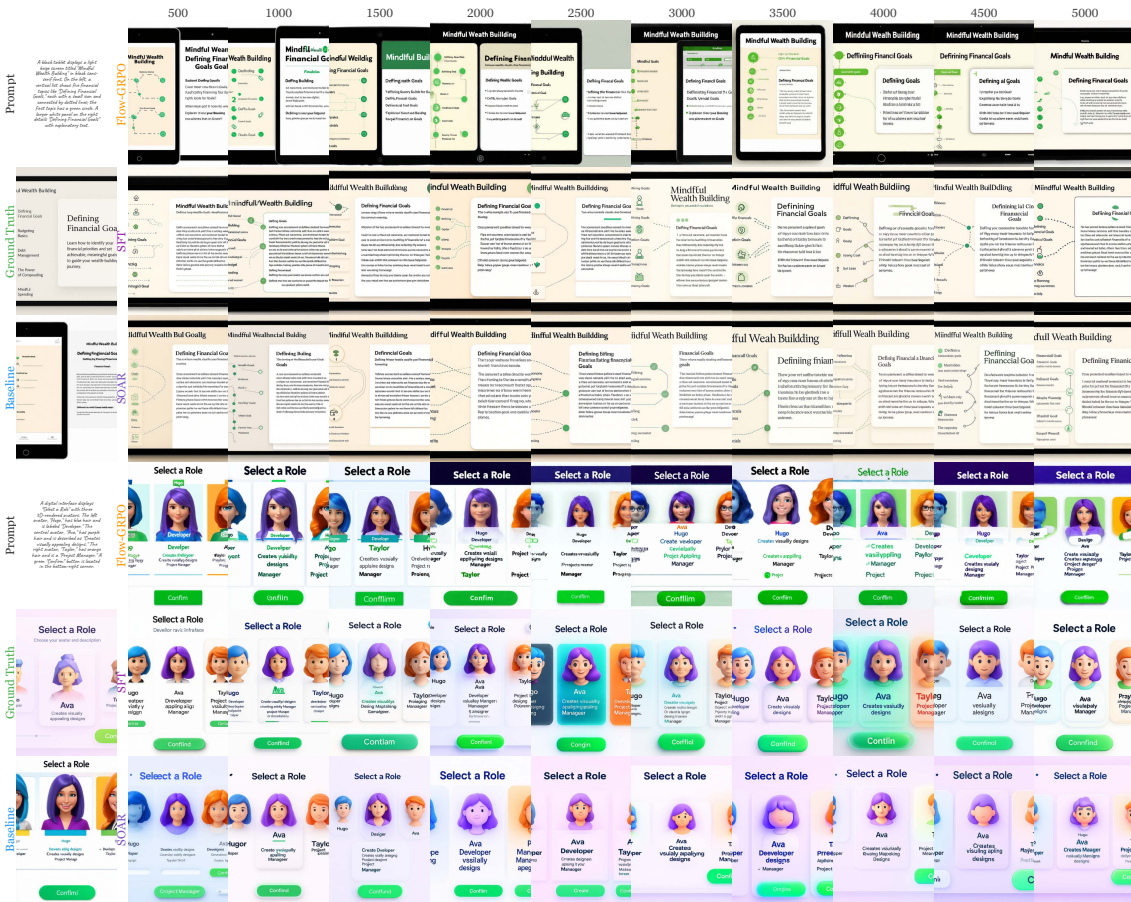


Figure 6: Training visualization on **WebUI** data. SOAR accurately captures interface elements, shadow effects, and fine-grained stylistic details.

Q4: How should the noise weighting $w(\sigma)$ be designed? The correction target $v_{\text{corr}} = (z_{\sigma_t} - z_0) / \sigma_t$ has a denominator σ_t that becomes small at low noise levels, amplifying the gradient magnitude. The current implementation inherits the base flow matching weight $w(\sigma)$, which was designed for the standard velocity target and does not specifically account for this amplification. A dedicated weighting schedule, for example one that down-weights the correction loss at very low σ to prevent gradient explosion or that up-weights mid-noise levels where the semantic-vs-detail trade-off is most active, could improve training stability and metric balance. We leave this investigation to future work.

3.6 Qualitative Visualization

Figures 4–6 present training-time visualizations across three data domains. The *high-aesthetic* subset (Figure 4) spans portraits, landscapes, and anime; as training progresses, SOAR produces increasingly coherent global compositions while preserving fine detail in faces, lighting, and textures. The *poster* (Figure 5) and *WebUI* (Figure 6) subsets test more structured generation tasks that demand precise layout, typographic placement, shadow rendering, and stylistic consistency. Across all three domains, SOAR demonstrates high learning efficiency and accuracy: the dense per-timestep correction signal enables the model to absorb not only semantic structure but also the subtle visual properties, including style, spatial hierarchy, specular effects, and drop shadows, that distinguish professional-quality outputs from generic generations. These are precisely the fine-grained attributes that a sparse terminal reward would struggle to credit to specific denoising steps, yet SOAR captures them through direct trajectory-level supervision.

4 Related Work

4.1 Diffusion Models and Flow Matching

Diffusion models generate data by learning to reverse a noise-corruption process (Ho et al., 2020; Song et al., 2021). Latent diffusion (Rombach et al., 2022) moves this process into a compressed latent space, enabling high-resolution synthesis. Flow matching (Lipman et al., 2023; Liu et al., 2023) reformulates generation as learning a velocity field along a linear interpolation between noise and data, yielding efficient ODE-based sampling. The rectified-flow variant (Liu et al., 2023) is adopted by current state-of-the-art systems including SD3.5 (Esser et al., 2024) and FLUX (Labs, 2024), and the DiT architecture (Peebles & Xie, 2023) has become the standard backbone. Our work builds on this flow-matching foundation and addresses a limitation of the training procedure, not the architecture.

4.2 Post-Training for Diffusion Models

Post-training methods can be broadly grouped into four categories. *Supervised fine-tuning* continues the flow matching or diffusion objective on curated data to improve specific capabilities such as text rendering or compositional accuracy. While simple and stable, SFT inherits the exposure-bias limitation discussed in Section 2.2. *Reward-based optimization* uses differentiable reward models such as ImageReward (Xu et al., 2023), HPS (Wu et al., 2023b;a), and PickScore to directly backpropagate preference signals into the generator. *DPO-style methods* (Wallace et al., 2024) adapt direct preference optimization to diffusion models by constructing positive and negative sample pairs and adjusting their relative likelihoods. In the flow-matching setting, however, the paired samples typically lie on different interpolation paths, lacking the geometric structure that SOAR exploits. DiffusionNFT (Zheng et al., 2026) extends this idea to the online setting by splitting model generations into positive and negative subsets according to reward and optimizing an implicit policy improvement direction on the forward process via flow matching, bypassing likelihood estimation entirely. *RL-style methods* treat denoising as an MDP and apply policy gradients. Flow-GRPO (Liu et al., 2025) introduces GRPO to flow matching via an ODE-to-SDE conversion, achieving GenEval accuracy of 95% on SD3.5-M. SimpleAR (Wang et al., 2025a) and T2I-R1 (Jiang et al., 2025) explore similar ideas for autoregressive and reasoning-augmented generators. Our work is positioned earlier in the post-training stack: rather than using reward optimization as the first tool, SOAR directly repairs the generator’s off-trajectory denoising behavior before any reward signal is introduced.

4.3 Exposure Bias in Sequential Generation

Exposure bias was first identified in autoregressive language modeling, where models are trained with teacher forcing but must condition on their own predictions at test time (Bengio et al., 2015). Scheduled sampling (Bengio et al., 2015) and related curriculum strategies partially mitigate this gap by occasionally substituting model predictions for ground-truth tokens during training.

In diffusion models the same mismatch occurs along the denoising axis. Ning et al. (2023) show that adding small perturbations to the training input (“input perturbation”) improves sample quality by exposing the model to slightly off-distribution states. Ning et al. (2024) provide a formal analysis of the exposure-bias effect in diffusion training and propose an auxiliary objective to reduce the compounding error. These works diagnose the problem and offer training-time regularization; SOAR goes further by constructing on-policy off-trajectory states from the model’s own rollout and supervising the correction explicitly, providing a more direct remedy that naturally integrates into the post-training pipeline.

4.4 External Correction and Reasoning-Based Control

A complementary line of work improves generation quality through external feedback loops rather than weight updates. Self-correcting LLM-controlled diffusion (Wu et al., 2024), Idea2Img (Yang et al., 2024b), dynamic prompt optimization (Hao et al., 2023; Mo et al., 2024; Mañas et al., 2024), reasoning-augmented re-prompting (Wu et al., 2025; Yang et al., 2024a), and chain-of-thought prompt rewriting (Wang et al., 2025b) leverage multimodal language models to iteratively refine prompts or select among candidate outputs. These methods are valuable when the generator weights are frozen, but they do not modify the nearby off-trajectory regions visited during inference.

SOAR is complementary: it targets the generator parameters directly, improving the base model that external correction methods build upon.

5 Conclusion

We have proposed SOAR, a post-training method that replaces standard SFT as a stronger first stage directly following pretraining in the diffusion model stack. By identifying exposure bias, the distributional mismatch between ground-truth training states and model-induced inference states, as a unifying cause of many persistent generation failures, SOAR provides a direct remedy: it constructs off-trajectory states from the model’s own rollout, re-noises them, and supervises the denoiser with an analytically derived correction target anchored to the original clean sample.

SOAR combines the desirable properties of both SFT and RL while avoiding their respective weaknesses. Like SFT, its supervision is dense and analytically derived, requiring no reward model. Like RL, it trains on states the model actually encounters, making it genuinely on-policy. Unlike RL, the correction signal acts at the exact timestep where the deviation occurs, eliminating the credit-assignment problem entirely. Experiments on SD3.5-Medium confirm that SOAR improves both rule-based and model-based metrics over SFT, achieves monotonic reward improvement on curated data subsets, and outperforms explicit RL in final metric value without access to a reward function.

Several directions remain open. First, although our results show uniform metric improvements, we have not yet evaluated the effect on generation *diversity* (e.g., via LPIPS or Vendi Score); the trajectory-correction bias toward training data may narrow the output distribution, and understanding this trade-off is important. Second, the noise-dependent weight $w(\sigma)$ is currently inherited from the base flow matching schedule; a dedicated analysis of how to weight the correction loss across noise levels could further improve the method. Finally, the bias-correction principle is not specific to image generation: whenever a flow-based or diffusion generator follows a multi-step trajectory, the same mechanism applies. Extending SOAR to video generation, 3D synthesis, and model distillation is a natural next step.

6 Acknowledgements

We would like to thank Zhenxi Li, Yixuan Shi, Tingting Gao for their valuable inputs and suggestions.

A Derivation and Training Details

This appendix provides the formal derivation of SOAR from the conditional optimal-transport structure of rectified flow. We first establish the transport-ray geometry (A.1), formalize the exposure bias as a distributional shift (A.2), derive the correction target from the clean-endpoint condition (A.3), connect the per-sample loss to distribution matching (A.4), and give the full loss aggregation and detailed algorithm (A.5).

A.1 Rectified Flow and Conditional Transport

Rectified flow (Liu et al., 2023) learns a velocity field that generates a straight-line probability path from the noise distribution $p_1 = \mathcal{N}(0, I)$ to the data distribution $p_0 = q(z_0)$. Each training pair (z_0, z_1) with $z_0 \sim q(z_0)$ and $z_1 \sim \mathcal{N}(0, I)$ defines a *transport ray*, the linear path

$$z_t = (1 - t)z_0 + tz_1, \quad t \in [0, 1]. \quad (16)$$

The *conditional velocity* along this ray is constant:

$$u(z_t | z_0, z_1) = z_1 - z_0. \quad (17)$$

The flow matching objective trains $v_\theta(z_t, c, t)$ to approximate the *marginal velocity*, i.e., the conditional expectation of u given the noisy state:

$$u_t(z_t) = \mathbb{E}[z_1 - z_0 | z_t] = \frac{z_t - \mathbb{E}[z_0 | z_t]}{t}. \quad (18)$$

The second equality follows from Eq. equation 16. The model’s velocity prediction at any state z and noise level σ implies a *clean-endpoint map*:

$$\hat{z}_0(z, \sigma) = z - \sigma \cdot v_\theta(z, c, \sigma). \quad (19)$$

This map is central to SOAR: both the on-trajectory and off-trajectory losses can be understood as requiring \hat{z}_0 to land on the correct clean sample z_0 .

A.2 Exposure Bias as Distributional Shift

During training, the model observes states drawn from the *ground-truth* (on-trajectory) distribution:

$$p_\sigma^{\text{data}}(z) = \int \delta((1 - \sigma)z_0 + \sigma z_1)(z) q(z_0) \mathcal{N}(z_1) dz_0 dz_1. \quad (20)$$

The SFT objective minimizes the velocity error under this distribution:

$$\mathcal{L}_{\text{SFT}} = \mathbb{E}_{z \sim p_\sigma^{\text{data}}} [\|v_\theta(z, \sigma) - u_\sigma(z)\|^2]. \quad (21)$$

During inference, the model solves the ODE $dz/d\sigma = v_\theta(z, \sigma)$ from $\sigma=1$ to $\sigma=0$. The resulting state at noise level σ is

$$\hat{z}_\sigma = z_1 + \int_1^\sigma v_\theta(\hat{z}_s, c, s) ds, \quad (22)$$

and its distribution $p_\sigma^\theta(z)$ is defined implicitly by this ODE. Since each state depends on the model’s previous predictions, any velocity error at an earlier step shifts all subsequent states.

Error accumulation. Consider a single Euler step from σ_0 to $\sigma_1 = \sigma_0 + \Delta\sigma$ (with $\Delta\sigma < 0$ during denoising). Let $\epsilon(\sigma_0) = v_\theta(z_{\sigma_0}, \sigma_0) - u_{\sigma_0}(z_{\sigma_0})$ denote the velocity error. The state deviation after one step is

$$\Delta z = |\Delta\sigma| \cdot \|\epsilon(\sigma_0)\|. \quad (23)$$

Over K Euler steps, the total deviation satisfies

$$\|\hat{z}_0 - z_0^{\text{ideal}}\| \leq \sum_{k=1}^K \frac{1}{K} \|\epsilon(\sigma_k)\| + (\text{higher-order cross terms}). \quad (24)$$

Even if each $\|\epsilon\|$ is small, the sum can become large because errors at early (high-noise) steps also shift the states at which later predictions are evaluated, creating a compounding effect. This is precisely the exposure-bias phenomenon: the model is trained on p_σ^{data} but evaluated on p_σ^θ , and the gap grows with the number of sampling steps.

A.3 SOAR Correction via Conditional Optimal Transport

SOAR addresses the exposure bias by expanding the training distribution from p^{data} to $p^{\text{data}} \cup p^{\text{rollout}}$, where p^{rollout} consists of states the model actually generates during a short rollout. We now formalize the construction and the correction target.

A.3.1 Off-Trajectory State Construction

Starting from a training pair (z_0, z_1, c) and the on-trajectory state $z_{\sigma_{t_0}} = (1 - \sigma_{t_0})z_0 + \sigma_{t_0}z_1$, we compute a stop-gradient CFG rollout velocity:

$$v_{\text{cfg}} = \text{sg}[v_{\theta}(z_{\sigma_{t_0}}, \emptyset, t_0) + w_{\text{cfg}}(v_{\theta}(z_{\sigma_{t_0}}, c, t_0) - v_{\theta}(z_{\sigma_{t_0}}, \emptyset, t_0))], \quad (25)$$

where \emptyset denotes the null condition and $\text{sg}[\cdot]$ prevents gradient flow. A single ODE step produces

$$\hat{z}_{\sigma_{t_1}} = z_{\sigma_{t_0}} + (\sigma_{t_1} - \sigma_{t_0})v_{\text{cfg}}, \quad t_1 = \max(t_0 - 1/K, 0). \quad (26)$$

The state $\hat{z}_{\sigma_{t_1}}$ deviates from the ideal $z_{\sigma_{t_1}}^{\text{ideal}} = (1 - \sigma_{t_1})z_0 + \sigma_{t_1}z_1$ by

$$\delta = \hat{z}_{\sigma_{t_1}} - z_{\sigma_{t_1}}^{\text{ideal}} = (\sigma_{t_1} - \sigma_{t_0})(v_{\text{cfg}} - (z_1 - z_0)). \quad (27)$$

This deviation is proportional to $|\sigma_{t_1} - \sigma_{t_0}| = 1/K$ and to the CFG-adjusted velocity error, both of which are bounded in practice.

We then construct auxiliary states by re-noising $\hat{z}_{\sigma_{t_1}}$ toward the noise endpoint z_1 . For an auxiliary noise level $\sigma_{t'} \in [\sigma_{t_1}, 1]$:

$$\alpha = \frac{\sigma_{t'} - \sigma_{t_1}}{1 - \sigma_{t_1}}, \quad (28)$$

$$z_{\sigma_{t'}} = (1 - \alpha)\hat{z}_{\sigma_{t_1}} + \alpha z_1. \quad (29)$$

A.3.2 Geometric Insight: Same-Noise Re-Noising

A critical design choice is that re-noising uses the **same** z_1 as the forward process, rather than drawing fresh Gaussian noise. This has a precise geometric consequence.

The ideal state at noise level $\sigma_{t'}$ on the original transport ray is $z_{\sigma_{t'}}^{\text{ideal}} = (1 - \sigma_{t'})z_0 + \sigma_{t'}z_1$. Writing the auxiliary state from Eq. equation 29 and substituting the deviation δ from Eq. equation 27:

$$\begin{aligned} z_{\sigma_{t'}} &= (1 - \alpha)(z_{\sigma_{t_1}}^{\text{ideal}} + \delta) + \alpha z_1 \\ &= \underbrace{(1 - \alpha)z_{\sigma_{t_1}}^{\text{ideal}} + \alpha z_1}_{\text{ideal state at } \sigma_{t'}} + (1 - \alpha)\delta. \end{aligned} \quad (30)$$

Therefore:

$$\|z_{\sigma_{t'}} - z_{\sigma_{t'}}^{\text{ideal}}\| = (1 - \alpha)\|\delta\|. \quad (31)$$

This bound has two important implications:

1. The deviation from the ideal ray is *strictly bounded* by the one-step rollout error $\|\delta\|$ and *shrinks* as $\alpha \rightarrow 1$ (i.e., as the auxiliary noise level approaches pure noise). At $\alpha = 1$, the auxiliary state coincides with z_1 regardless of the rollout error.
2. Because the auxiliary state remains close to the transport ray ($z_0 \leftrightarrow z_1$), the original z_0 is still the uniquely correct clean-endpoint target under the learned coupling. The state has not drifted to a different mode of the data distribution where a different z'_0 would be more appropriate.

If instead we used fresh noise $z'_1 \sim \mathcal{N}(0, I)$, the auxiliary state would be $z'_{\sigma_{t'}} = (1 - \alpha)\hat{z}_{\sigma_{t_1}} + \alpha z'_1$. This state lies on a *different* interpolation path ($z_0 \leftrightarrow z'_1$), and the ideal target from the perspective of this path would involve z'_1 , not the original z_1 . Using z_0 as the correction anchor for such a state introduces a systematic bias that grows with α and with the distance $\|z_1 - z'_1\|$. The ablation in Section 3.4 confirms that shared z_1 outperforms fresh noise on rule-based metrics.

A.3.3 Deriving the Correction Target

We derive the correction target following the same logic as Section 2.3.3, with full algebraic detail.

From local trajectory matching to goal consistency. The most direct way to correct a drifted state is to require that, after a small step Δt , the off-trajectory state z'_σ reconverges with the on-trajectory state z_σ :

$$z_\sigma + \Delta t \cdot v_{\text{gt}} = z'_\sigma + \Delta t \cdot v_{\text{corr}}. \quad (32)$$

However, the step size Δt introduces an ambiguity: different choices yield different correction targets, and the optimal Δt depends on the downstream trajectory. We resolve this by requiring both states to reach the same final endpoint z_0 , eliminating Δt entirely. On the ideal trajectory, $z_\sigma = (1-\sigma)z_0 + \sigma z_1$ with $v_{\text{gt}} = z_1 - z_0$ satisfies

$$z_\sigma - \sigma \cdot v_{\text{gt}} = z_0. \quad (33)$$

Imposing the same goal consistency condition on the off-trajectory state gives

$$z'_\sigma - \sigma \cdot v_{\text{corr}} = z_0, \quad (34)$$

which yields the closed-form correction target:

$$v_{\text{corr}} = \frac{z'_\sigma - z_0}{\sigma}. \quad (35)$$

On-trajectory verification. When $z'_\sigma = z_\sigma$ (no deviation), substituting $z_\sigma = (1-\sigma)z_0 + \sigma z_1$ into Eq. equation 35:

$$v_{\text{corr}} = \frac{(1-\sigma)z_0 + \sigma z_1 - z_0}{\sigma} = z_1 - z_0 = v_{\text{gt}}. \quad (36)$$

This recovers the standard flow matching target, confirming that the correction objective generalizes the SFT loss.

Off-trajectory case. For an auxiliary state $z_{\sigma'}$ from Eq. equation 29, which deviates from the ideal ray by $(1-\alpha)\delta$ (Eq. 30), the correction target differs from v_{gt} by:

$$v_{\text{corr}} - v_{\text{gt}} = \frac{z_{\sigma'} - z_{\sigma'}^{\text{ideal}}}{\sigma'} = \frac{(1-\alpha)\delta}{\sigma'}. \quad (37)$$

This correction term is proportional to the rollout deviation δ , scaled by the interpolation factor $(1-\alpha)$ and the noise level σ' . It is the dense, per-timestep signal that steers the model back toward z_0 from the off-trajectory states it actually visits during inference.

A.4 Distribution Matching Interpretation

We can frame the combined SOAR objective in distributional terms. For a given training pair (z_0, z_1) , the model's clean-endpoint prediction at state z with noise level σ is a point mass:

$$\mu_\theta(z, \sigma) = \delta_{z_0(z, \sigma)} = \delta_{z - \sigma v_\theta(z, \sigma)}. \quad (38)$$

The target is also a point mass: $\mu^* = \delta_{z_0}$. The 2-Wasserstein distance between them is:

$$W_2^2(\mu_\theta, \mu^*) = \|\hat{z}_0(z, \sigma) - z_0\|^2 = \sigma^2 \|v_\theta(z, \sigma) - v^*(z, \sigma)\|^2. \quad (39)$$

The SFT objective minimizes W_2^2 in expectation over $z \sim p_\sigma^{\text{data}}$:

$$\mathcal{L}_{\text{SFT}} = \mathbb{E}_{z_0, z_1, \sigma} [W_2^2(\mu_\theta(z_\sigma^{\text{data}}, \sigma), \delta_{z_0})]. \quad (40)$$

The SOAR objective extends this to both on-trajectory and off-trajectory states:

$$\mathcal{L}_{\text{SOAR}} = \mathbb{E}_{z_0, z_1, \sigma} \left[\underbrace{W_2^2(\mu_\theta(z_\sigma^{\text{data}}, \sigma), \delta_{z_0})}_{\text{on-trajectory}} + \lambda \underbrace{W_2^2(\mu_\theta(z_\sigma^{\text{roll}}, \sigma), \delta_{z_0})}_{\text{off-trajectory}} \right], \quad (41)$$

where z_σ^{roll} denotes an auxiliary state from Eq. equation 29. In practice, the σ^2 factor from Eq. equation 39 is absorbed into the noise-dependent weight $w(\sigma)$, and the expectation is approximated by batch-level summation.

The key difference from SFT is that the expectation now covers $p^{\text{data}} \cup p^{\text{rollout}}$ instead of p^{data} alone. By training on states the model actually visits during inference, SOAR directly closes the exposure-bias gap identified in Section A.2.

Algorithm 2 Detailed SOAR training procedure (with optional SDE branches)

Require: velocity field v_θ , condition c , correction weight λ
 rollout CFG scale w_{cfg} , ODE/SDE branch count M
 auxiliary points per branch N , rollout step count K

- 1: **for** each training batch **do**
- 2: Sample clean latent z_0 , Gaussian noise $z_1 \sim \mathcal{N}(0, I)$, and training time t_0
- 3: Compute σ_{t_0} and construct $z_{\sigma_{t_0}} = (1 - \sigma_{t_0})z_0 + \sigma_{t_0}z_1$
- 4: $v_{\text{on}} \leftarrow v_\theta(z_{\sigma_{t_0}}, c, t_0)$; $v_{\text{gt}} \leftarrow z_1 - z_0$
- 5: $\mathcal{L}_{\text{main}} += w(\sigma_{t_0})\|v_{\text{on}} - v_{\text{gt}}\|^2$; $N_{\text{main}} \leftarrow B$; $N_{\text{aux}} \leftarrow 0$
- 6: **if** $\lambda > 0$ and $N > 0$ **then**
- 7: Compute $v_{\text{cfg}} \leftarrow \text{sg}[v_{\text{uncond}} + w_{\text{cfg}}(v_{\text{cond}} - v_{\text{uncond}})]$
- 8: $t_1 \leftarrow \max(t_0 - 1/K, 0)$; $\sigma_{t_1} \leftarrow \sigma(t_1)$
- 9: **Path 0 (ODE):** $\hat{z}_{\sigma_{t_1}}^{(0)} \leftarrow z_{\sigma_{t_0}} + (\sigma_{t_1} - \sigma_{t_0})v_{\text{cfg}}$
- 10: **if** $M > 1$ and $t_1 > 0$ **then** ▷ optional SDE branches
- 11: **for** $m = 1, \dots, M-1$ **do**
- 12: $\hat{z}_{\sigma_{t_1}}^{(m)} \leftarrow \Psi(z_{\sigma_{t_0}}, v_{\text{cfg}}, \sigma_{t_0}, \sigma_{t_1}; \eta)$
- 13: **end for**
- 14: **end if**
- 15: **for** each branch endpoint $\hat{z}_{\sigma_{t_1}}^{(m)}$, $m = 0, \dots, M'-1$ **do**
- 16: **for** $n = 1, \dots, N$ **do**
- 17: Sample $\sigma_{t'} \sim \text{Uniform}[\sigma_{t_1}, 1]$
- 18: $\alpha \leftarrow (\sigma_{t'} - \sigma_{t_1}) / (1 - \sigma_{t_1})$
- 19: $z_{\sigma_{t'}} \leftarrow (1 - \alpha)\hat{z}_{\sigma_{t_1}}^{(m)} + \alpha z_1$
- 20: $v_{\text{off}} \leftarrow v_\theta(z_{\sigma_{t'}}, c, t')$; $v_{\text{corr}} \leftarrow (z_{\sigma_{t'}} - z_0) / \sigma_{t'}$
- 21: $\mathcal{L}_{\text{aux}} += \lambda w(\sigma_{t'})\|v_{\text{off}} - v_{\text{corr}}\|^2$; $N_{\text{aux}} += |\text{batch}|$
- 22: **end for**
- 23: **end for**
- 24: **end if**
- 25: All-reduce $N_{\text{main}}, N_{\text{aux}}$ across workers
- 26: $\mathcal{L}_{\text{total}} \leftarrow (\mathcal{L}_{\text{main}} + \mathcal{L}_{\text{aux}}) / (N_{\text{main}} + \lambda N_{\text{aux}})$
- 27: Update θ using $\nabla_\theta \mathcal{L}_{\text{total}}$
- 28: **end for**

A.5 Loss Aggregation and Practical Details

For a batch of size B with P valid auxiliary points in total, let $w(\sigma)$ denote the noise-dependent loss weight inherited from the base flow matching schedule. The per-sample on-trajectory and off-trajectory losses are:

$$\ell_{\text{base}}^{(b)} = w(\sigma_{t_0}^{(b)})\|v_\theta(z_{\sigma_{t_0}^{(b)}}, c^{(b)}, t_0^{(b)}) - v_{\text{gt}}^{(b)}\|^2, \quad \ell_{\text{aux}}^{(p)} = w(\sigma_{t'}^{(p)})\|v_\theta(z_{\sigma_{t'}^{(p)}}, c^{(p)}, t'^{(p)}) - v_{\text{corr}}^{(p)}\|^2, \quad (42)$$

where both norms are averaged over the latent dimension d . The combined objective aggregates all supervised items and normalizes once:

$$\mathcal{L}_{\text{total}} = \frac{\sum_{b=1}^B \ell_{\text{base}}^{(b)} + \lambda \sum_{p=1}^P \ell_{\text{aux}}^{(p)}}{B + \lambda P}. \quad (43)$$

Under distributed training, B and P are synchronized across workers via all-reduce before normalization to ensure consistent gradient scaling.

In the default configuration ($M=1$, ODE-only), the algorithm reduces to Algorithm 1 in the main text. The optional SDE branches ($M > 1$) apply a stochastic one-step operator Ψ (e.g., coefficient-preserving sampling with noise scale η) and are evaluated in the ablation study (Section 3.4). In either case, the core supervision pattern is the same: the model is trained on both the ideal ground-truth state and the nearby off-trajectory states that its own rollout can produce.

References

- Samy Bengio, Oriol Vinyals, Navdeep Jaitly, and Noam Shazeer. Scheduled sampling for sequence prediction with recurrent neural networks. In *Advances in Neural Information Processing Systems (NeurIPS)*, 2015.
- Patrick Esser, Sumith Kulal, Andreas Blattmann, Rahim Entezari, Jonas Müller, Harry Saini, Yam Levi, Dominik Lorenz, Axel Sauer, Frederic Boesel, et al. Scaling rectified flow transformers for high-resolution image synthesis. In *Forty-first international conference on machine learning (ICML)*, 2024.
- Yaru Hao, Zewen Chi, Li Dong, and Furu Wei. Optimizing prompts for text-to-image generation. *Advances in Neural Information Processing Systems*, 36:66923–66939, 2023.
- Jonathan Ho, Ajay Jain, and Pieter Abbeel. Denoising diffusion probabilistic models. *Advances in neural information processing systems (NeurIPS)*, 33:6840–6851, 2020.
- Kaiyi Huang, Kaiyue Sun, Enze Xie, Zhenguo Li, and Xihui Liu. T2i-compbench: A comprehensive benchmark for open-world compositional text-to-image generation. *Advances in Neural Information Processing Systems (NeurIPS)*, 36:78723–78747, 2023.
- Dongzhi Jiang, Ziyu Guo, Renrui Zhang, Zhuofan Zong, Hao Li, Le Zhuo, Shilin Yan, Pheng-Ann Heng, and Hongsheng Li. T2i-r1: Reinforcing image generation with collaborative semantic-level and token-level cot. *arXiv preprint arXiv:2505.00703*, 2025.
- Weijie Kong, Qi Tian, Zijian Zhang, Rox Min, Zuozhuo Dai, Jin Zhou, Jiangfeng Xiong, Xin Li, Bo Wu, Jianwei Zhang, et al. Hunyuanvideo: A systematic framework for large video generative models. *arXiv preprint arXiv:2412.03603*, 2024.
- Black Forest Labs. Flux, 2024. URL <https://github.com/black-forest-labs/flux>.
- Yaron Lipman, Ricky T. Q. Chen, Heli Ben-Hamu, Maximilian Nickel, and Matt Le. Flow matching for generative modeling. In *International Conference on Learning Representations (ICLR)*, 2023.
- Jie Liu, Gongye Liu, Jiajun Liang, Yangguang Li, Jiaheng Liu, Xintao Wang, Pengfei Wan, Di Zhang, and Wanli Ouyang. Flow-grpo: Training flow matching models via online rl. *Advances in Neural Information Processing Systems (NeurIPS)*, 2025.
- Xingchao Liu, Chengyue Gong, and Qiang Liu. Flow straight and fast: Learning to generate and transfer data with rectified flow. In *International Conference on Learning Representations (ICLR)*, 2023.
- Oscar Mañas, Pietro Astolfi, Melissa Hall, Candace Ross, Jack Urbanek, Adina Williams, Aishwarya Agrawal, Adriana Romero-Soriano, and Michal Drozdal. Improving text-to-image consistency via automatic prompt optimization. *arXiv preprint arXiv:2403.17804*, 2024.
- Wenyi Mo, Tianyu Zhang, Yalong Bai, Bing Su, Ji-Rong Wen, and Qing Yang. Dynamic prompt optimizing for text-to-image generation. In *Proceedings of the IEEE/CVF Conference on Computer Vision and Pattern Recognition*, pp. 26627–26636, 2024.
- Mang Ning, Enver Sangineto, Angelo Porrello, Simone Calderara, and Rita Cucchiara. Input perturbation reduces exposure bias in diffusion models. In *International Conference on Machine Learning (ICML)*, 2023.
- Mang Ning, Mingxiao Li, Jianlin Su, Albert Ali Salah, and Itir Onal Ertugrul. Elucidating the exposure bias in diffusion models. In *International Conference on Learning Representations (ICLR)*, 2024.
- William Peebles and Saining Xie. Scalable diffusion models with transformers. In *Proceedings of the IEEE/CVF international conference on computer vision (ICCV)*, pp. 4195–4205, 2023.
- Dustin Podell, Zion English, Kyle Lacey, Andreas Blattmann, Tim Dockhorn, Jonas Müller, Joe Penna, and Robin Rombach. SDXL: Improving latent diffusion models for high-resolution image synthesis. In *The Twelfth International Conference on Learning Representations (ICLR)*, 2024. URL <https://openreview.net/forum?id=di52zR8xgf>.

-
- Robin Rombach, Andreas Blattmann, Dominik Lorenz, Patrick Esser, and Björn Ommer. High-resolution image synthesis with latent diffusion models. In *Proceedings of the IEEE/CVF conference on computer vision and pattern recognition (CVPR)*, pp. 10684–10695, 2022.
- Chitwan Saharia, William Chan, Saurabh Saxena, Lala Li, Jay Whang, Emily L Denton, Kamyar Ghasemipour, Raphael Gontijo Lopes, Burcu Karagol Ayan, Tim Salimans, et al. Photorealistic text-to-image diffusion models with deep language understanding. *Advances in neural information processing systems (NeurIPS)*, 35:36479–36494, 2022.
- Yang Song, Jascha Sohl-Dickstein, Diederik P Kingma, Abhishek Kumar, Stefano Ermon, and Ben Poole. Score-based generative modeling through stochastic differential equations. In *International Conference on Learning Representations (ICLR)*, 2021. URL <https://openreview.net/forum?id=PXTIG12RRHS>.
- Bram Wallace, Meihua Dang, Rafael Rafailov, Linqi Zhou, Aaron Lou, Senthil Purushwalkam, Stefano Ermon, Caiming Xiong, Shafiq Joty, and Nikhil Naik. Diffusion model alignment using direct preference optimization. In *Proceedings of the IEEE/CVF Conference on Computer Vision and Pattern Recognition (CVPR)*, pp. 8228–8238, 2024.
- Junke Wang, Zhi Tian, Xun Wang, Xinyu Zhang, Weilin Huang, Zuxuan Wu, and Yu-Gang Jiang. Simplear: Pushing the frontier of autoregressive visual generation through pretraining, sft, and rl. *arXiv preprint arXiv:2504.11455*, 2025a.
- Linqing Wang, Ximing Xing, Yiji Cheng, Zhiyuan Zhao, Donghao Li, Tiankai Hang, Jiale Tao, Qixun Wang, Ruihuang Li, Comi Chen, Xin Li, Mingrui Wu, Xincheng Deng, Shuyang Gu, Chunyu Wang, and Qinglin Lu. Promptenhancer: A simple approach to enhance text-to-image models via chain-of-thought prompt rewriting. *arXiv preprint arXiv:2509.04545*, 2025b.
- Mingrui Wu, Lu Wang, Pu Zhao, Fangkai Yang, Jianjin Zhang, Jianfeng Liu, Yuefeng Zhan, Weihao Han, Hao Sun, Jiayi Ji, et al. Reprompt: Reasoning-augmented reprompting for text-to-image generation via reinforcement learning. *arXiv preprint arXiv:2505.17540*, 2025.
- Tsung-Han Wu, Long Lian, Joseph E Gonzalez, Boyi Li, and Trevor Darrell. Self-correcting llm-controlled diffusion models. In *Proceedings of the IEEE/CVF Conference on Computer Vision and Pattern Recognition*, pp. 6327–6336, 2024.
- Xiaoshi Wu, Yiming Hao, Keqiang Sun, Yixiong Chen, Feng Zhu, Rui Zhao, and Hongsheng Li. Human preference score v2: A solid benchmark for evaluating human preferences of text-to-image synthesis. *arXiv preprint arXiv:2306.09341*, 2023a.
- Xiaoshi Wu, Keqiang Sun, Feng Zhu, Rui Zhao, and Hongsheng Li. Human preference score: Better aligning text-to-image models with human preference. In *Proceedings of the IEEE/CVF International Conference on Computer Vision (ICCV)*, pp. 2096–2105, October 2023b.
- Jiazheng Xu, Xiao Liu, Yuchen Wu, Yuxuan Tong, Qinkai Li, Ming Ding, Jie Tang, and Yuxiao Dong. Imagereward: Learning and evaluating human preferences for text-to-image generation. *Advances in Neural Information Processing Systems (NeurIPS)*, 36:15903–15935, 2023.
- Ling Yang, Zhaochen Yu, Chenlin Meng, Minkai Xu, Stefano Ermon, and Bin Cui. Mastering text-to-image diffusion: Recaptioning, planning, and generating with multimodal llms. In *Forty-first International Conference on Machine Learning*, 2024a.
- Zhengyuan Yang, Jianfeng Wang, Linjie Li, Kevin Lin, Chung-Ching Lin, Zicheng Liu, and Lijuan Wang. Idea2img: Iterative self-refinement with gpt-4v for automatic image design and generation. In *European Conference on Computer Vision*, pp. 167–184. Springer, 2024b.
- Kaiwen Zheng, Huayu Chen, Haotian Ye, Haoxiang Wang, Qinsheng Zhang, Kai Jiang, Hang Su, Stefano Ermon, Jun Zhu, and Ming-Yu Liu. Diffusionnft: Online diffusion reinforcement with forward process. In *International Conference on Learning Representations (ICLR)*, 2026.